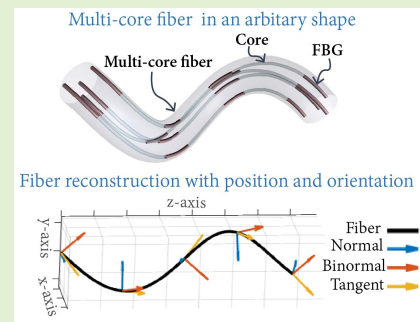


# Pose Measurement of Flexible Medical Instruments Using Fiber Bragg Gratings in Multi-Core Fiber

Fouzia Khan<sup>1</sup>, Abdulhamit Donder, Stefano Galvan, Ferdinando Rodriguez y Baena<sup>2</sup>, and Sarthak Misra<sup>1</sup>

**Abstract**—Accurate navigation of flexible medical instruments like catheters require the knowledge of its pose, that is its position and orientation. In this paper multi-core fibers inscribed with fiber Bragg gratings (FBG) are utilized as sensors to measure the pose of a multi-segment catheter. A reconstruction technique that provides the pose of such a fiber is presented. First, the measurement from the Bragg gratings are converted to strain then the curvature is deduced based on those strain calculations. Next, the curvature and the Bishop frame equations are used to reconstruct the fiber. This technique is validated through experiments where the mean error in position and orientation is observed to be less than 4.69 mm and 6.48 degrees, respectively. The main contributions of the paper are the use of Bishop frames in the reconstruction and the experimental validation of the acquired pose.

**Index Terms**—Fiber Bragg grating, bio-medical, robotics, shape sensing, medical instrument, 3D reconstruction, multi-core optical fiber, Bishop frames, parallel transport.



## I. INTRODUCTION

FLEXIBLE medical instruments are frequently used for procedures in cardiology and urology. Accurate navigation of these instruments require spatial information such as the pose, as shown in Figure 1. Conventionally, fluoroscopy or ultrasound are used to monitor these instruments, even though both methods have their drawbacks [1]. Fluoroscopy exposes the patient to contrast agents and to radiation. In addition, the workflow of the procedure is disrupted to allow the medical personnel time to retreat during imaging. On the

Manuscript received May 2, 2020; accepted May 4, 2020. Date of publication May 8, 2020; date of current version August 14, 2020. This work was supported by the European Union's Horizon 2020 Research and Innovation Programme under Grant 688279 (EDEN 2020). The work of Abdulhamit Donder was supported by the Republic of Turkey. The associate editor coordinating the review of this article and approving it for publication was Dr. Ioannis Raptis. (Corresponding author: Fouzia Khan.)

Fouzia Khan and Sarthak Misra are with the Surgical Robotics Laboratory, Department of Biomedical Engineering, University of Groningen and the University of Medical Center Groningen, 9713 GZ Groningen, The Netherlands, and also with the Department of Biomechanical Engineering, Engineering Technology, University of Twente, 7522 NB Enschede, The Netherlands (e-mail: f.khan@utwente.nl).

Abdulhamit Donder, Stefano Galvan, and Ferdinando Rodriguez y Baena are with the Mechatronics in Medicine Laboratory, Department of Mechanical Engineering, Imperial College London, London SW7 2AZ, U.K.

Digital Object Identifier 10.1109/JSEN.2020.2993452

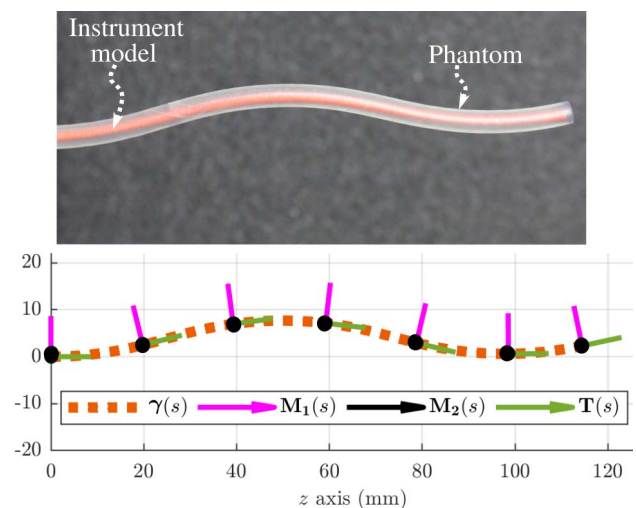


Fig. 1. Top: A flexible instrument model placed in a vascular phantom. Bottom: Ideal reconstruction of the instrument along the arc length  $s$  with position given as a curve,  $\gamma(s)$ , and the orientation as a frame  $\{M_1(s), M_2(s), T(s)\}$ .

other hand, ultrasound images have low resolution and the instruments can cause artifacts [2]. Thus, there is a need to develop imaging and other sensing techniques to acquire the spatial information of flexible instruments.

In the literature there are studies that used endoscopic images for retrieving spatial information of flexible instruments. Relink *et al.* used markers on an instrument and a state estimator to acquire the position of the instrument [3]. Cabaras *et al.* used feature detection along with learning methods to detect the pose of a flexible instrument from monocular endoscopic images [4]. Although these studies show the feasibility of acquiring the instrument tip position from endoscopic images; they require an unobstructed view of the surgical site. Thus, they are difficult to use in practice and are applicable only to procedures that use endoscopes. An alternative technology that mitigates the requirement of unobstructed view is electromagnetic (EM) tracking. However, it has a limited workspace and the tracking accuracy degrades significantly in the presence of electronic and metallic instruments [5]. Thus, EM tracking is better suited for controlled environments than clinical settings.

Another approach for acquiring spatial information is using optical fibers. This is an attractive approach due to the compatibility of the sensors with the medical environment. Optical fibers are biocompatible, nontoxic, immune to electromagnetic interference and sterilizable [6]. In addition, they are small and highly flexible, and thus can be easily integrated into medical instruments [1], [7]. Sareh *et al.* have used the bend sensitivity of optical fibers to get the pose of the instrument tip [8]. This approach leads to low-cost sensing hardware, but multiple fibers are required that must be routed in a specific manner and it has a complex calibration procedure. The required routing renders it inapplicable to instruments like catheters and needles. These issues can be mitigated by employing fiber Bragg grating (FBG) sensors in the optical fibers.

Moore *et al.* calculated the shape of a multi-core fiber with FBG sensors using Frenet-Serret equations [9]. Numerous other studies have used FBG sensors for sensing shape of flexible instruments such as colonoscope, needle and catheter. Xinhua *et al.* acquired the shape of a colonoscope from optical fibers with FBG sensors in order to reduce the probability of loop formation during colonoscopy [10]. Park *et al.* placed optical fibers with two sets of FBG sensors on a needle to provide tip deflection, bend profile and temperature compensation [11]. Roesthuis *et al.* acquired the 3D shape of a needle using four sets of FBG sensors in optical fibers [12]. Khan *et al.* reconstructed the shape of a multi-segment catheter in 3D space using multi-core fibers with six sets of FBGs in each fiber [13]. Lastly, Henken *et al.* calculated the needle tip deflection based on strains derived from measurements from two sets of FBG sensors [14]. Nevertheless, these studies have focused on acquiring only the position of the instrument.

The study presented in this paper extends the use of FBG sensors for acquiring the orientation of an instrument in addition to its position. This information can be utilized for improving the navigation accuracy of flexible medical instruments. The sensors are written in multi-core fibers instead of being written on several single-core fibers due to the space restriction in these instruments. The contributions of this study include the use of Bishop frames in the reconstruction and validation of the acquired pose. The reconstruction technique

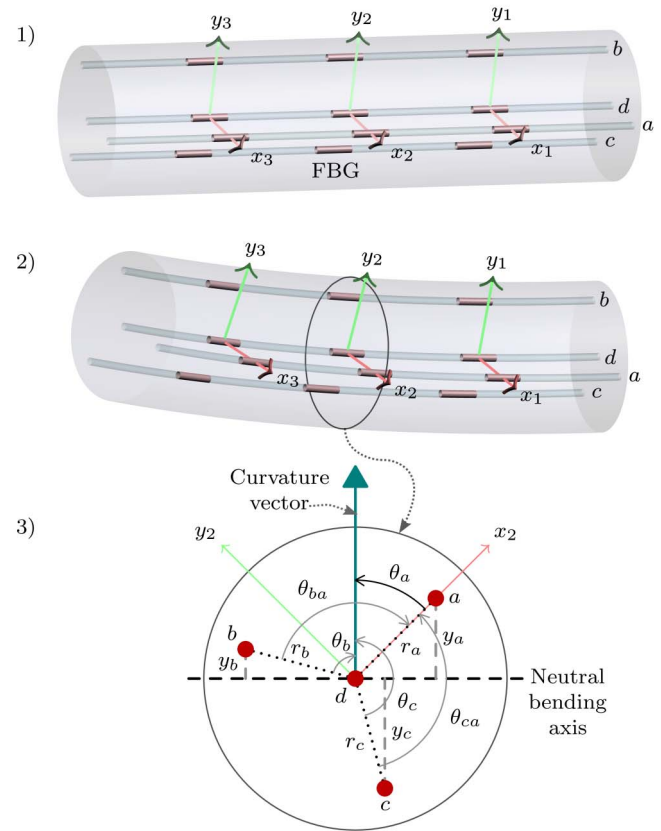


Fig. 2. 1) A segment of the multi-core fiber in its initial configuration. The four cores of the fiber are labeled  $a, b, c$  and  $d$ . Three sets of fiber Bragg gratings (FBG) sensors and their local frames for curvature vector calculation are shown. 2) The segment of the multi-core fiber in a bent configuration. 3) The fiber cross section at the second set of FBG sensors when the fiber is bent. The variables required for the curvature vector calculation are illustrated;  $y_i \in \mathbb{R}_{>0}$  (where  $i \in a, b, c, d$ ) is the perpendicular distance from the FBG sensor on core  $i$  to the neutral bending axis;  $r_i \in \mathbb{R}_{>0}$  is the radial distance from the center to core  $i$ ;  $\theta_i \in (-\pi, \pi]$  is the angle from  $r_i$  to the curvature vector;  $\theta_{ba}$  is the angle between  $r_b$  and  $r_a$  and  $\theta_{ca}$  is the angle between  $r_c$  and  $r_a$ .

is described in Section II, followed by the experiments, discussion and conclusion in Section III, IV and V, respectively.

## II. THEORY

This section outlines the technique for reconstructing a multi-core fiber with FBG sensors. The fiber is modeled as a regular unit-speed space curve that is reconstructed in Euclidean space using curvature vectors and Bishop frame equations [15], [16]. The curvature vectors of the fiber are calculated at every FBG sensor set using strains that are derived from the wavelength measurements of the sensors in the set. Description of FBG sensor and the derivation of strain values is given in Section II-A, followed by an explanation of the curvature vector calculation in Section II-B. Lastly, the reconstruction using Bishop frame equations is presented in Section II-C.

### A. Fiber Bragg Grating for Strain Measurement

An FBG reflects back a narrow band of wavelengths from the optical input and transmits the rest. The reflection is due

to the grating being a periodic variation in the refractive index of the fiber over a short segment. The properties of the grating are altered by strain and temperature; as a result the reflected wavelength band shifts when a change in strain or change in temperature is experienced by the grating [17]. The wavelength which has the highest reflection is called the Bragg wavelength,  $\lambda_B \in \mathbb{R}_{>0}$ . It is related to strain and temperature on the grating according to the following equation [18]:

$$\ln \frac{\lambda_B}{\lambda_{B0}} = S(\epsilon - \epsilon_0) + \Sigma(T - T_0), \quad (1)$$

where,  $S \in \mathbb{R}$  is the gauge factor;  $\Sigma \in \mathbb{R}$  is the temperature sensitivity;  $\epsilon \in \mathbb{R}$  is the strain and  $T \in \mathbb{R}$  is temperature.  $\lambda_{B0}$ ,  $\epsilon_0$  and  $T_0$  are the initial values of the Bragg wavelength, strain and temperature, respectively.

In this study, the initial Bragg wavelength  $\lambda_{B0}$  is collected when the fiber is straight so that the fiber is strain-free and  $\epsilon_0$  can be assumed to be zero. In addition, an FBG sensor is placed in the central core of the fiber so that the strain on the sensor is zero when the fiber is bent and the term  $\Sigma(T - T_0)$  can be acquired from it. The value of  $\lambda_B$  is measured and  $S$  is a known constant. Thus, the strain on an FBG sensor can be calculated.

The next section presents the details on acquiring the curvature vectors of the fiber given the arrangement of the FBG sensors within the fiber and their strain values.

### B. Curvature Vector

The curve representing the fiber can be reconstructed if the curvature vectors are known for the complete length of the curve. In this study, the curvature vectors are acquired from sets of FBG sensors placed along the length of the multi-core fiber. Each set of FBG sensors contains four co-located FBGs, one in the center core and three in the outer cores as shown in Figure 2. An orthogonal frame is attached to each FBG set such that the  $x$  and  $y$  axis are on the fiber cross section and the  $x$  axis is from the center of the fiber to one of the outer core, see Figure 2. The curvature vector for a set is calculated with respect to the allocated orthogonal frame by utilizing the relation between curvature and strain provided by the theory of bending mechanics [19]. The strain experienced by the FBG sensors on the outer cores is proportional to their perpendicular distance from the neutral bending axis. Adapting the sign convention for the strain to be positive for tension and negative for compression, the relation between strain and curvature is as follows:

$$\epsilon_i(s) = -\kappa(s)y_i(s) = -\kappa(s)r_i \cos(\theta_i(s)), \quad (2)$$

where,  $s \in \mathbb{R}$  is the parameter for the arc length of the fiber and is defined in the interval  $\Omega \subset \mathbb{R}$  such that  $\Omega = (0, L)$ ;  $L \in \mathbb{R}_{>0}$  is the length of the fiber.  $\epsilon_i(s) \in \mathbb{R}_{>0}$  is the strain on the FBG in core  $i \in \{a, b, c, d\}$ ;  $\kappa(s) \in \mathbb{R}_{>0}$  is the magnitude of curvature;  $y_i(s) \in \mathbb{R}$  is the perpendicular distance from the FBG in core  $i$  to the neutral axis;  $r_i \in \mathbb{R}_{>0}$  is the radial distance from the center to core  $i$ ; and  $\theta_i(s) \in (-\pi, \pi]$  is the angle from  $r_i$  to the curvature vector. These variables are illustrated in Figure 2.3.

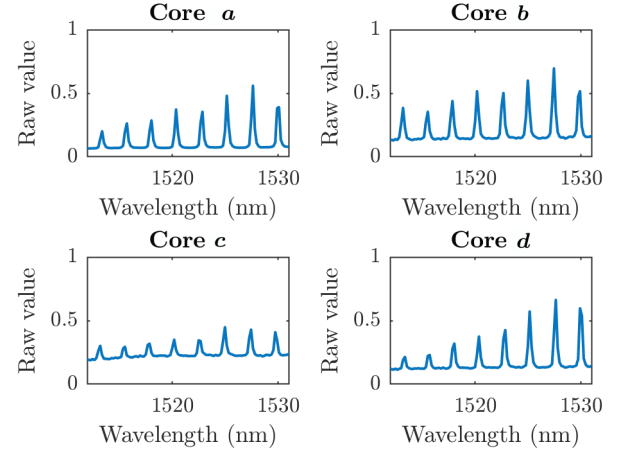


Fig. 3. Spectra from the four cores labeled *a*, *b*, *c*, and *d* of a fiber as provided by the software of the interrogator FBG-scan 804D (FBGS International NV (Geel, Belgium)). The raw values in the y-axis of the plots are the output of the interrogator and they are the result of normalization by the saturation value of the interrogator's light sensors.

The curvature value  $\kappa(s)$  and the angle  $\theta_a(s)$  are the magnitude and angle of the curvature vector for the set of FBG sensors at arc length  $s$  of the fiber. The location of the FBG sensor set on the fiber is known *a priori*;  $\kappa(s)$  and  $\theta_s(s)$  are acquired from the four FBG sensor measurements at a location  $s$  using the following method. Let  $\xi_i(s) = \ln \frac{\lambda_{Bi}(s)}{\lambda_{B0i}(s)}$ , where  $\lambda_{Bi}(s)$  is the measured Bragg wavelength and  $\lambda_{B0i}(s)$  is the Bragg wavelength when no strain is applied on the fiber so that  $\epsilon_0 = 0$ , then from (1)

$$\xi_i(s) = S\epsilon_i(s) + c_i(s), \quad (3)$$

where  $c_i(s) = \Sigma(T_i(s) - T_{0i}(s))$  and is assumed to be the same in all the FBG sensors that are in one set due to their close proximity. The strain value  $\epsilon_d$  from the FBG sensor in core *d* is set to be zero because it is on the neutral bending axis, thus  $\xi_d(s) = c_i(s)$ . Given these assumptions and substituting (2) into (3) the following set of equations hold:

$$\xi_a(s) - \xi_d(s) = -S\kappa(s)r_a \cos(\theta_a(s)), \quad (4)$$

$$\xi_b(s) - \xi_d(s) = -S\kappa(s)r_b \cos(\theta_b(s) + \theta_{ba}), \quad (5)$$

$$\xi_c(s) - \xi_d(s) = -S\kappa(s)r_c \cos(\theta_c(s) + \theta_{ca}), \quad (6)$$

where,  $\theta_{ba}$  is the angle between  $r_b$  and  $r_a$ ; similarly,  $\theta_{ca}$  is the angle between  $r_c$  and  $r_a$ . Applying trigonometric angle sum identities, Equations (4)-(6) can be represented as a matrix equation

$$\xi(s) = \mathbf{C}v(s), \quad (7)$$

where,

$$\xi(s) = \begin{bmatrix} \xi_a(s) - \xi_d(s) \\ \xi_b(s) - \xi_d(s) \\ \xi_c(s) - \xi_d(s) \end{bmatrix}, \mathbf{C} = \begin{bmatrix} -Sr_a & 0 \\ -Sr_b \cos(\theta_{ba}) & Sr_b \sin(\theta_{ba}) \\ -Sr_c \cos(\theta_{ca}) & Sr_c \sin(\theta_{ca}) \end{bmatrix},$$

$$v(s) = \begin{bmatrix} v_1(s) \\ v_2(s) \end{bmatrix} = \begin{bmatrix} \kappa(s) \cos(\theta_a(s)) \\ \kappa(s) \sin(\theta_a(s)) \end{bmatrix}.$$

The components of  $v(s)$  can be solved using the pseudo-inverse of  $\mathbf{C}$

$$v(s) = \mathbf{C}^\dagger \xi(s), \quad (8)$$



then using the definition of  $\mathbf{v}(s)$  from (7),

$$\kappa(s) = \sqrt{v_1^2(s) + v_2^2(s)}, \quad (9)$$

$$\theta_a(s) = \text{atan2}(v_2(s), v_1(s)). \quad (10)$$

The parameters  $\kappa(s)$  and  $\theta_a(s)$  give the curvature vector of the fiber for one set of FBG sensors at location  $s$ . This calculation can be repeated for all the FBG sensor sets on the fiber to get the curvature vectors which are required for the reconstruction as explained in the next subsection.

### C. Reconstruction

The Bishop frame is used to reconstruct the curve that represents the fiber. It is selected over the more common Frenet-Serret frame because it has less restrictions on the curve than the Frenet-Serret frame [16]. More specifically, Bishop frame is valid for curves that are twice differentiable whereas Frenet-Serret frame require three times differentiability. This enables Bishop frames to be better suited for curves that have local linearity or discontinuity in curvature; as demonstrated in simulation by Shiyuan *et al.* [20]. Let  $\mathbf{y}(s) \in \mathbb{R}^3$  be the position vector of the curve. The frame at  $s$  consists of three orthonormal vectors  $\mathbf{T}(s) \in \mathbb{R}^3$ ,  $\mathbf{M}_1(s) \in \mathbb{R}^3$ , and  $\mathbf{M}_2(s) \in \mathbb{R}^3$ . The derivatives of the position and the frame with respect to the arc length of the curve are as follows [16]:

$$\frac{d\mathbf{y}(s)}{ds} = \mathbf{T}(s), \quad (11)$$

$$\frac{d\mathbf{T}(s)}{ds} = k_1(s)\mathbf{M}_1(s) + k_2(s)\mathbf{M}_2(s), \quad (12)$$

$$\frac{d\mathbf{M}_1(s)}{ds} = -k_1(s)\mathbf{T}(s), \quad (13)$$

$$\frac{d\mathbf{M}_2(s)}{ds} = -k_2(s)\mathbf{T}(s). \quad (14)$$

In this study, the parameters  $k_1(s) \in \mathbb{R}$  and  $k_2(s) \in \mathbb{R}$  are calculated from the values of the curvature vector  $\kappa(s)$  and  $\theta_a(s)$  using the following relation:

$$k_1(s) = v_1(s) = \kappa(s)\cos(\theta_a(s)), \quad (15)$$

$$k_2(s) = v_2(s) = \kappa(s)\sin(\theta_a(s)). \quad (16)$$

This gives values of  $k_1(s)$  and  $k_2(s)$  at the locations of the FBG sensor sets. The values of  $k_1(s)$  and  $k_2(s)$  in between the FBG sensor set locations are estimated using linear interpolation. The interpolated values are denoted as  $\tilde{k}_1(s)$  and  $\tilde{k}_2(s)$ . The position  $\mathbf{y}(s)$  and the frame  $\{\mathbf{M}_1(s), \mathbf{M}_2(s), \mathbf{T}(s)\}$  are solved using the following matrix form of (11)-(14):

$$\frac{d}{ds}\mathbf{X}(s) = \mathbf{X}(s)\mathbf{A}(s), \quad (17)$$

where,

$$\mathbf{X}(s) = \begin{bmatrix} \mathbf{T}(s) & \mathbf{M}_1(s) & \mathbf{M}_2(s) & \mathbf{y}(s) \\ 0 & 0 & 0 & 1 \end{bmatrix}, \quad (18)$$

$$\mathbf{A}(s) = \begin{bmatrix} 0 & -\tilde{k}_1(s) & -\tilde{k}_2(s) & 1 \\ \tilde{k}_1(s) & 0 & 0 & 0 \\ \tilde{k}_2(s) & 0 & 0 & 0 \\ 0 & 0 & 0 & 0 \end{bmatrix}. \quad (19)$$

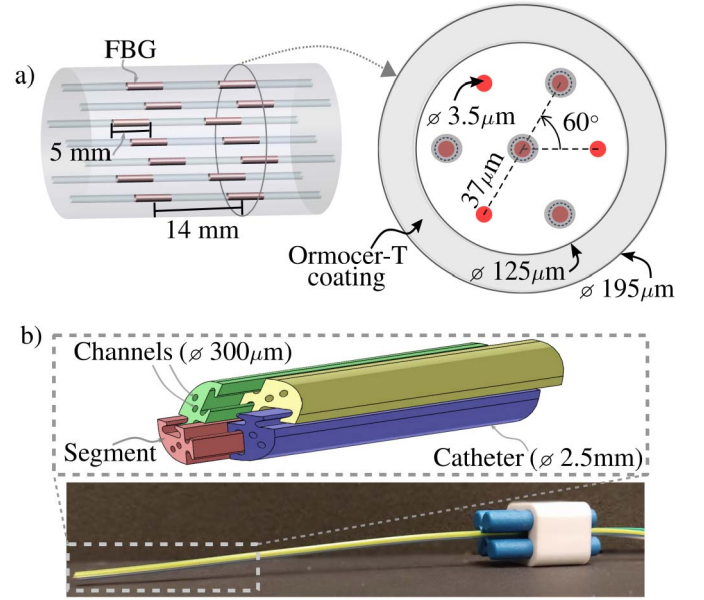


**Fig. 4.** a) Cross-section and side view of the fibers utilized for the experiments. Each fiber has seven cores with eight groups of fiber Bragg grating (FBG) sensors. Two groups of sensors and the fiber cross-section are shown. A set of sensors used for the curvature vector calculations consists of four out of the seven sensors, as highlighted on the cross-section with gray discs. b) Photograph of the four-segment catheter used in the experiments along with an inset that shows the tip. Each segment can move independently in the axial direction and has two channels that are utilized for an electromagnetic (EM) sensor and a fiber.

The discretized solution to (17) assuming  $\mathbf{A}(s)$  is held constant between two consecutive values of  $\tilde{k}_1(s)$ , and  $\tilde{k}_2(s)$  is given as:

$$\mathbf{X}(s + \Delta s) = \mathbf{X}(s) \exp(\mathbf{A}(s) \Delta s). \quad (20)$$

The tip pose is given by  $\mathbf{X}(L)$ , where  $L$  is the length of the fiber. The initial position is assumed to be  $\mathbf{y}(0) = [0 \ 0 \ 0]^T$  and the orientation to be  $\mathbf{M}_1(0) = [1 \ 0 \ 0]^T$ ,  $\mathbf{M}_2(0) = [0 \ 1 \ 0]^T$ ,  $\mathbf{T}(0) = [0 \ 0 \ 1]^T$ .

The reconstruction technique presented in Section II is empirically validated in the next Section.

### III. EXPERIMENTS

Three different experiments are conducted to validate the reconstructed pose using the technique presented in Section II. Particularly, the tip pose is used for validation since the reconstruction error is the largest there due to the accumulation of error over the length in (20). The difference in tip pose between the reconstruction and the ground truth is calculated using three measures; one measure is the magnitude of the error in position  $r_e \in \mathbb{R}$ , the second is the angle between the orientation vector  $\phi_e \in \mathbb{R}$ , and the last measure is the difference in the rotation angles about the orientation vector  $\theta_e \in \mathbb{R}$ . The error measures are calculated as follows:

$$r_e(k) = \|\mathbf{r}(k) - \mathbf{r}_{gt}(k)\| \quad (21)$$

$$\phi_e(k) = \cos^{-1} \left( \frac{\mathbf{v}_{gt}(k) \cdot \mathbf{v}(k)}{\|\mathbf{v}_{gt}(k)\| \|\mathbf{v}(k)\|} \right) \quad (22)$$

$$\theta_e(k) = \|\theta(k) - \theta_{gt}(k)\| \quad (23)$$

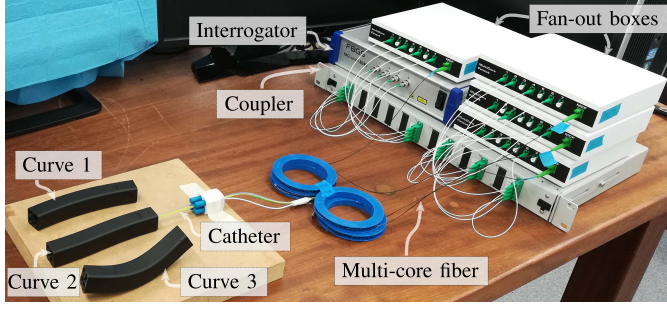


Fig. 5. Setup for Experiment 1. The catheter is sensorized with four multi-core fibers that have fiber Bragg gratings (FBG); each catheter segment has one fiber. The experiment utilizes four multi-core fibers, fan-out boxes, interrogator, coupler, catheter, and three molds.

TABLE I

THE CURVATURE AND TORSION ALONG THE ARC LENGTH OF THE CENTERLINE IN THE MOLDS USED FOR EXPERIMENT 1

Configuration	Curvature ( $\text{mm}^{-1}$ )	Torsion ( $\text{mm}^{-1}$ )
Curve 1: Single bend	constant: $3.3e^{-3}$	constant: 0
Curve 2: Double bend	linear: $2.5e^{-3}$ to $-2.5e^{-3}$	constant: 0
Curve 3: Space curve	constant: $1.0e^{-2}$	constant: $2.2e^{-2}$

where,  $k \in \mathbb{Z}_{\geq 0}$  represents the sample of the data;  $\mathbf{r}(k) \in \mathbb{R}^3$  is the reconstructed tip position;  $\mathbf{r}_{gt}(k) \in \mathbb{R}^3$  is the ground truth of the tip position;  $\mathbf{v}(k) \in \mathbb{R}^3$  is the reconstructed tip orientation vector,  $\mathbf{v}_{gt}(k) \in \mathbb{R}^3$  is the true orientation vector,  $\theta(k) \in \mathbb{R}$  is the angle of rotation about the reconstructed orientation vector and  $\theta_{gt}(k) \in \mathbb{R}$  is the angle of rotation about the true orientation vector. Details on the hardware and software for the experiments are given in Section III-A. Descriptions of the three experiments and the results are given in Sections III-B, III-C and III-D. Registration between the reference frame of the fibers and the reference frame of the ground truth is conducted for each experiment. A set of points in each frame is collected and the transformation between the frames is solved using least square estimation [21].

### A. Setup

The hardware for the three experiments consists of a four-segment catheter, four multi-core fibers with eight sets of FBG sensors, an interrogator, four fan out boxes and a coupler. In addition, Experiment 1 includes 3D printed molds; Experiment 2 and 3 uses four EM sensors placed at the tip of the four segments; lastly, Experiment 3 utilizes a gelatin phantom and an actuation unit. The setup for Experiments 1, 2 and 3 are shown in Figures 5, 7 and 9, respectively.

The FBG sensors are written using the Draw Tower Grating technique on all the cores at eight locations on each of the four fibers [22]. The spectra from a strain-free fiber are shown in Figure 3. The nominal Bragg wavelength differ between consecutive FBG sensors by 2.4 nm and the wavelength range on the four fibers are 1513–1529.8 nm, 1532.2–1549 nm, 1551.4–1568.2 nm, and 1570.6–1587.4 nm. As shown in Figure 4a, every sensor is 5 mm long and the sensor sets are 14 mm apart which means the sensorized section of each fiber is 103 mm. The core and the cladding of the fiber

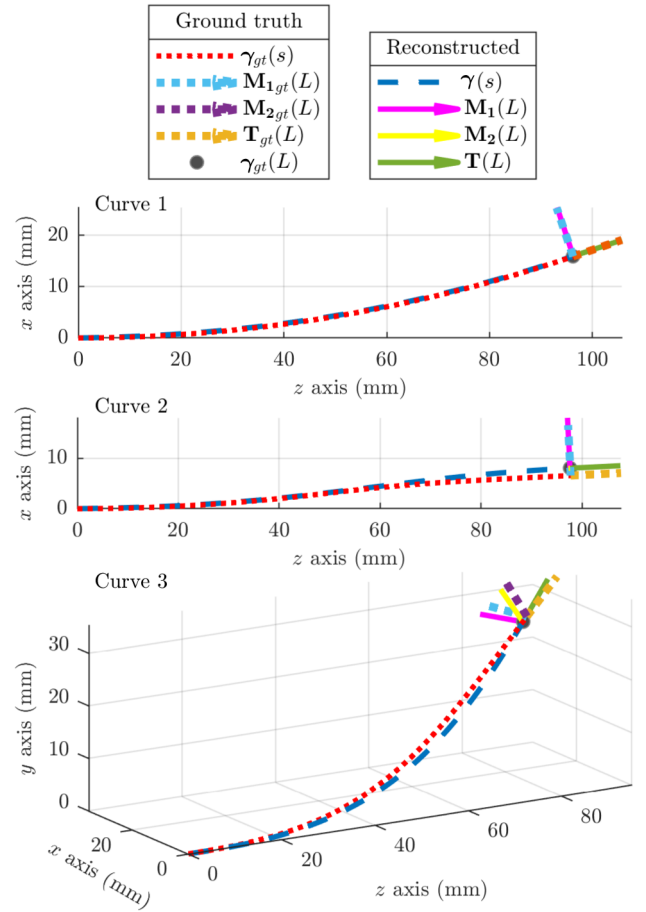


Fig. 6. The ground truth and the reconstruction plots of the three curves from one sample in Experiment 1. In the legend,  $\gamma(s) \in \mathbb{R}^3$ , is the reconstructed curve, where  $s \in \mathbb{R}$  is the arc length parameter.  $M_1(L) \in \mathbb{R}^3$ ,  $M_2(L) \in \mathbb{R}^3$  and  $T(L) \in \mathbb{R}^3$  represent the orientation at the curve's tip. Similarly,  $\gamma_{gt}(s) \in \mathbb{R}^3$ ,  $M_{1_{gt}}(L) \in \mathbb{R}^3$ ,  $M_{2_{gt}}(L) \in \mathbb{R}^3$ ,  $T_{gt}(L) \in \mathbb{R}^3$  are the analogous values from the ground truth. Lastly,  $\gamma_{gt}(L) \in \mathbb{R}^3$  is the ground truth curve's tip position.

are composed of fused silica and their refractive indices are 1.454 and 1.444, respectively. The operating temperature range of the fiber is  $-20^\circ\text{C}$  to  $200^\circ\text{C}$  [23]. FBGS International NV (Geel, Belgium) supplied the fibers with FBG sensors, the value of the gauge factor  $S = 0.777$  in (1), the interrogator (FBG-scan 804D), four fan out boxes and a coupler [24].

The catheter is 2.5 mm in diameter and manufactured with medical-grade polymer by Xograph Healthcare Ltd. (Gloucestershire, United Kingdom). It is illustrated in Figure 4b. Further information on the catheter manufacturing procedure and material properties are given in Watts *et al.* [25]. The shape of the catheter can be controlled with the relative difference in the insertion length of the segments. The insertion of each catheter segment is controlled and executed by the actuation unit that is described in Watts *et al.* [25].

The EM sensor is part of the Aurora System from NDI Medical (Ontario, Canada), it is 0.3 mm in diameter and has five degrees of freedom which include position in three dimensions, pitch and yaw. The root mean square error of the EM sensors is 0.70 mm and  $0.20^\circ$  in position and orientation, respectively [26].

TABLE II

MEAN ( $\bar{r}_e$ ,  $\bar{\phi}_e$ ,  $\bar{\theta}_e$ ) AND STANDARD DEVIATION ( $\sigma_{r_e}$ ,  $\sigma_{\phi_e}$ ,  $\sigma_{\theta_e}$ ) OF THE ERROR IN CATHETER TIP POSE FROM (21), (22) AND (23) OVER THE SAMPLES COLLECTED FOR EACH CURVE IN EXPERIMENT 1

	Curve 1	Curve 2	Curve 3
$\bar{r}_e$ ( $\sigma_{r_e}$ ) (mm)	0.09 (0.03)	1.45 (0.06)	1.73 (0.05)
$\bar{\phi}_e$ ( $\sigma_{\phi_e}$ ) (degree)	1.01 (0.09)	0.66 (0.04)	0.37 (0.03)
$\bar{\theta}_e$ ( $\sigma_{\theta_e}$ ) (degree)	0.34 (0.06)	0.32 (0.05)	1.94 (0.06)

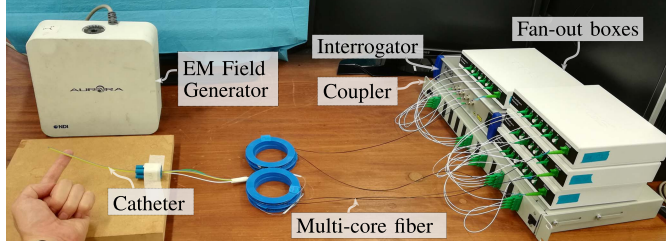


Fig. 7. Setup for Experiment 2. The catheter is sensorized with fiber Bragg gratings (FBG) inscribed multi-core fibers and electromagnetic (EM) sensors. The hardware utilized consists of four multi-core fibers, fan-out boxes, interrogator, coupler, four-segment catheter, four electromagnetic (EM) sensors and EM field generator.

The gelatin phantom is produced to mimic soft brain tissue from 4.5% by weight bovine gelatin [27]. The 3D printed molds and the actuation unit are designed and built in-house. The software used in the experiments is also developed in-house for Ubuntu 16.04.

### B. Experiment 1: Static Tests

A four-segment catheter with four fibers is placed in 3D printed molds and the reconstructed catheter tip pose is compared to the tip pose of the mold's centerline. Table I describes the curves that form the centerline of the three molds. Each fiber is reconstructed using (20) and the catheter's centerline is calculated as the mean of the reconstructed position and orientation of the fibers at particular arc lengths. Data from Curve 1 are used to solve for the transformation between the reconstruction frame and the ground truth frame.

The reconstruction of the catheter centerline is validated by the error in the tip pose. The error measures of (21), (22) and (23) are used where  $\mathbf{v}(k)$  is the axis and  $\theta(k)$  is the angle from the axis-angle representation of the tip orientation frame  $\{\mathbf{M}_1(L), \mathbf{M}_2(L), \mathbf{T}(L)\}$  and  $\mathbf{r}(k)$  is  $\boldsymbol{\gamma}(L)$  at sample  $k$ . Similarly, the ground truth values  $\mathbf{r}_{gt}(k)$ ,  $\theta_{gt}(k)$  and  $\mathbf{v}_{gt}(k)$  are acquired from the mold's centerline curve. For this experiment the ground truth values are constant for all samples. The mean of the error measures and the standard deviation given in Table II are over all samples. The reconstruction and the ground truth from a sample of the three curves are shown in Figure 6.

### C. Experiment 2: Dynamic Tests Conducted in Air

In this experiment, the catheter is moved in air by manually pushing on it from different directions. The objective is to validate the reconstruction by comparing the reconstructed

TABLE III

MEAN ( $\bar{r}_e$ ,  $\bar{\phi}_e$ ) AND STANDARD DEVIATION ( $\sigma_{r_e}$ ,  $\sigma_{\phi_e}$ ) OF THE FIBER TIP POSE ERROR ACCORDING TO (21) AND (22) OVER THE SAMPLES COLLECTED FROM ALL FOUR FIBERS DURING EXPERIMENT 2

	Trial 1	Trial 2	Trial 3
$\bar{r}_e$ ( $\sigma_{r_e}$ ) (mm)	2.20 (1.28)	2.95 (1.88)	2.89 (1.42)
$\bar{\phi}_e$ ( $\sigma_{\phi_e}$ ) (degree)	3.50 (1.38)	3.52 (1.10)	3.37 (1.27)

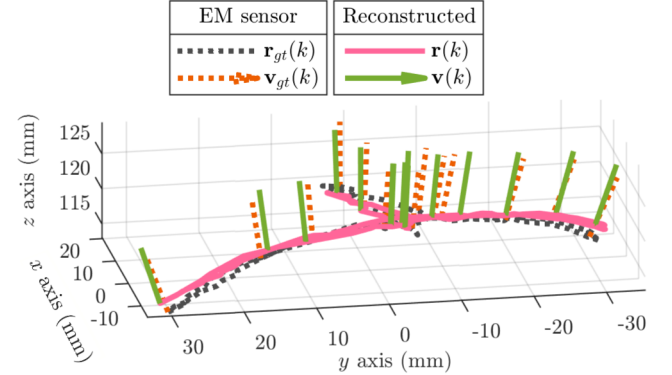


Fig. 8. The trajectory traced by an electromagnetic (EM) sensor and the corresponding fiber tip placed in the catheter during Trial 1. The orientation vectors at selected samples are also shown on the trajectory.  $k \in \mathbb{R}$  represents a sample in time,  $\mathbf{r}(k) \in \mathbb{R}^3$  is the fiber tip position,  $\mathbf{v}(k) \in \mathbb{R}^3$  is the fiber tip orientation vector.  $\mathbf{r}_{gt}(k) \in \mathbb{R}^3$  and  $\mathbf{v}_{gt}(k) \in \mathbb{R}^3$  are the position and orientation from the EM sensor, respectively.

fiber tip pose to an EM sensor pose. Each of the catheter's four segments is sensorized with a fiber and an EM sensor, which is placed at the segment's tip. The four fibers' tip pose from the reconstruction and the four EM sensors' pose are collected over time. The catheter is manually moved for three trials and an additional trial is conducted in order to solve for the transformation between the EM sensor frame and the reconstruction frame. The tip pose of each fiber is reconstructed using (20) and it is compared to the pose of the EM sensor in the same segment as the fiber. The error is calculated using (21) and (22) where,  $\mathbf{r}(k)$  is  $\boldsymbol{\gamma}(L)$  and  $\mathbf{v}(k)$  is  $\mathbf{T}(L)$  at sample  $k$ . The value for  $\mathbf{r}_{gt}(k)$  and  $\mathbf{v}_{gt}(k)$  are acquired from the EM sensor measurements. Since the EM sensors have 5 degrees of freedom, the rotation about the orientation axis is not available. Table III gives the mean and standard deviation of the error measures among all the segments over the duration of every trial. The trajectory of a fiber tip and of the corresponding EM sensor during the first trial is given in Figure 8.

### D. Experiment 3: Dynamic Tests Conducted in Gelatin

The catheter is inserted into a gelatin phantom that mimics soft brain tissue [25]. The aim is to validate the reconstruction when distributed force is applied along the catheter from the environment. The catheter is sensorized as in Experiment 2. Three insertions into the phantom are conducted; in the first insertion the catheter follows a straight path, in the second the catheter follows a single bend path and finally in the third, the catheter follows a double bend path. Each insertion is



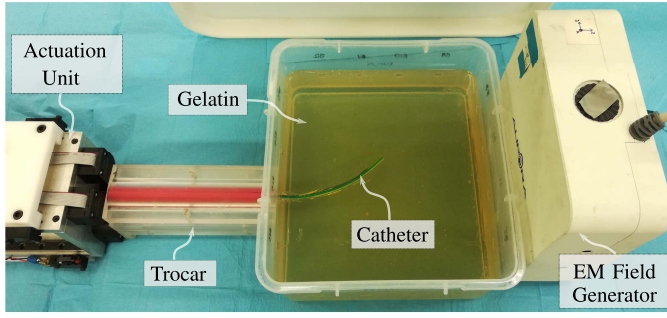


Fig. 9. Setup for Experiment 3. The catheter followed a single bend path. It is sensorized with multi-core fibers that have fiber Bragg gratings (FBG) and electromagnetic (EM) sensors. The experiment utilizes hardware from Experiment 2 and in addition requires an actuation unit, trocar to hold the catheter and gelatin phantom.

controlled by an actuation unit as described in Watts *et al.* so that the catheter follows the pre-determined path [25]. For each insertion, data from the FBG sensors in the fibers and the EM sensors are collected simultaneously.

The fiber tip is reconstructed using (20). The error between the reconstructed fiber tip pose and the EM sensor on the same catheter segment is calculated using (21) and (22) where the variables have the same assignment as in Experiment 2. The EM frame and the reconstruction frame are registered using data from a trial that constituted of manually moving the catheter in air. Figure 10 shows the plot of a catheter segment's tip trajectory during the second insertion which consisted of a single bend path. The mean and standard deviation of the error measures for the three insertions are given in Table IV.

#### IV. DISCUSSION

In the static experiments, the difference in error between this study and Khan *et al.* is possibly due to the different FBG inscription method utilized for the sensors. In this study Draw Tower Grating (DTG) technique is used whereas Khan *et al.* used a Phase Mask (PM) technique [13]. The DTG technique produced sensors with reflectivity of 3% of the input light whereas the PM technique produced sensors with reflectivity of at least 30%. The higher reflectivity of the sensors inscribed with PM technique could lead to more accurate detection of the Bragg wavelength, which would result in a lower reconstruction error. However, for the PM technique the fiber coating is removed before inscription, which made the fiber very fragile and unsuitable for dynamic experiments with gelatine or soft tissue. In the DTG technique the sensors are inscribed just after the fiber is drawn and before the coating is applied [28]. Since the original coating of the fiber remained intact the resulting fiber had high breakage strength, which is necessary for dynamic experiments. For this reason, sensors inscribed with DTG technique are utilized in this study.

In the dynamic experiments, the error may be caused by the fiber's motion relative to the catheter. The fibers are attached to the segments at a single point near the catheter base, so that they can be detached and reused. Thus, the fibers are free within the channel and can move relative to the catheter. The

TABLE IV

MEAN ( $\bar{r}_e$ ,  $\bar{\phi}_e$ ) AND STANDARD DEVIATION ( $\sigma_{r_e}$ ,  $\sigma_{\phi_e}$ ) OF THE FIBER TIP POSE ERROR ACCORDING TO (21) AND (22) FOR THE THREE INSERTIONS IN EXPERIMENT 3. THE MEAN AND STANDARD DEVIATION IS OVER ALL THE TIP POSE COLLECTED FROM THE FOUR FIBERS AND EM SENSORS DURING EACH INSERTION

	Insertion 1	Insertion 2	Insertion 3
$\bar{r}_e$ ( $\sigma_{r_e}$ ) (mm)	1.54 (1.34)	4.35 (2.17)	4.69 (2.81)
$\bar{\phi}_e$ ( $\sigma_{\phi_e}$ ) (degree)	2.85 (2.11)	6.48 (3.18)	3.49 (2.51)

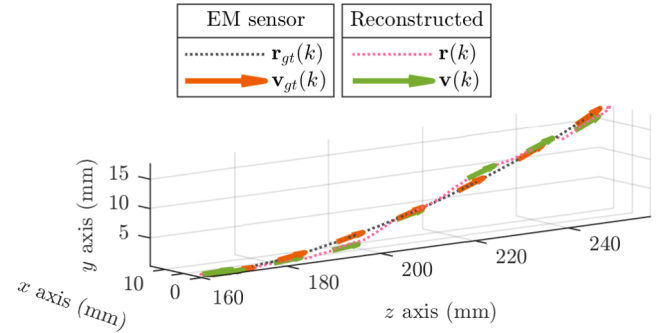


Fig. 10. The trajectory during insertion 2 of the electromagnetic (EM) sensor and the fiber tip from one of the catheter's segments.  $k \in \mathbb{R}$  represents a sample in time,  $r(k) \in \mathbb{R}^3$  is the fiber tip position, and  $v(k) \in \mathbb{R}^3$  is the fiber tip orientation vector.  $r_{gt}(k) \in \mathbb{R}^3$  and  $v_{gt}(k) \in \mathbb{R}^3$  are the position and orientation from the EM sensors, respectively.

error due to fiber motion may be reduced by incorporating a mechanics model of the catheter in the pose measurement.

#### V. CONCLUSION AND FUTURE WORK

A technique for acquiring the pose of a flexible instrument from FBG measurements is presented in the paper. The measurements from the FBG sensors are first converted to strain and then the curvature vectors are calculated at the locations on the fiber with co-located FBG sensors. The curvature calculation uses the strain values from the sensors and the theory of bending mechanics. Once the curvature is calculated, the fiber is reconstructed using Bishop Frames. The reconstruction provides the pose of the fiber along its arc length and the tip pose is validated in two dynamics experiments. The reconstruction of four fibers is utilized to deduce an instrument's tip pose which is validated in static experiments. The results from all the experiments show that the mean error in position is less than 4.69 mm and mean error in orientation is less than 6.48 degrees. Thus, acquiring the pose of a flexible instrument is feasible with FBG sensors in multi-core fiber. In future work, temperature sensing and temperature compensation using FBG sensors in multi-core fiber will be studied.

#### ACKNOWLEDGMENTS

The authors would like to thank Dr. Riccardo Secoli and Ms. Eloise Matheson for their help with Experiment 3. In addition, they appreciate the valuable feedback on the manuscript from Dr. Venkat Kalpathy Venkiteswaran and Mr. Jakub Sikorski.

## REFERENCES

- [1] D. Tosi, E. Schena, C. Molardi, and S. Korganbayev, "Fiber optic sensors for sub-centimeter spatially resolved measurements: Review and biomedical applications," *Opt. Fiber Technol.*, vol. 43, pp. 6–19, Jul. 2018.
- [2] C. Shi *et al.*, "Shape sensing techniques for continuum robots in minimally invasive surgery: A survey," *IEEE Trans. Biomed. Eng.*, vol. 64, no. 8, pp. 1665–1678, Aug. 2017.
- [3] R. Reilink, S. Stramigioli, and S. Misra, "Pose reconstruction of flexible instruments from endoscopic images using markers," in *Proc. IEEE Int. Conf. Robot. Autom.*, May 2012, pp. 2938–2943.
- [4] P. Cabras, F. Nageotte, P. Zanne, and C. Doignon, "An adaptive and fully automatic method for estimating the 3D position of bendable instruments using endoscopic images," *Int. J. Med. Robot. Comput. Assist. Surgery*, vol. 13, no. 4, p. e1812, Dec. 2017.
- [5] A. M. Franz, T. Haidegger, W. Birkfellner, K. Cleary, T. M. Peters, and L. Maier-Hein, "Electromagnetic tracking in medicine—A review of technology, validation, and applications," *IEEE Trans. Med. Imag.*, vol. 33, no. 8, pp. 1702–1725, Aug. 2014.
- [6] F. Taffoni, D. Formica, P. Saccomandi, G. Pino, and E. Schena, "Optical fiber-based MR-compatible sensors for medical applications: An overview," *Sensors*, vol. 13, no. 10, pp. 14105–14120, 2013.
- [7] B. Lee, "Review of the present status of optical fiber sensors," *Opt. Fiber Technol.*, vol. 9, no. 2, pp. 57–79, 2003.
- [8] S. Sareh, Y. Noh, M. Li, T. Ranzani, H. Liu, and K. Althoefer, "Macrobend optical sensing for pose measurement in soft robot arms," *Smart Mater. Struct.*, vol. 24, no. 12, Dec. 2015, Art. no. 125024.
- [9] J. P. Moore and M. D. Rogge, "Shape sensing using multi-core fiber optic cable and parametric curve solutions," *Opt. Express*, vol. 20, no. 3, pp. 2967–2973, Jan. 2012.
- [10] Y. Xinhua, W. Mingjun, and C. Xiaomin, "Deformation sensing of colonoscope on FBG sensor net," *Telkomnika Indonesian J. Elect. Eng.*, vol. 10, no. 8, pp. 2253–2260, 2012.
- [11] Y.-L. Park *et al.*, "Real-time estimation of 3-D needle shape and deflection for MRI-guided interventions," *IEEE/ASME Trans. Mechatronics*, vol. 15, no. 6, pp. 906–915, Dec. 2010.
- [12] R. J. Roesthuis, M. Kemp, J. J. van den Dobbelsteen, and S. Misra, "Three-dimensional needle shape reconstruction using an array of fiber Bragg grating sensors," *IEEE/ASME Trans. Mechatronics*, vol. 19, no. 4, pp. 1115–1126, Aug. 2014.
- [13] F. Khan, A. Denasi, D. Barrera, J. Madrigal, S. Sales, and S. Misra, "Multi-core optical fibers with Bragg gratings as shape sensor for flexible medical instruments," *IEEE Sensors J.*, vol. 19, no. 14, pp. 5878–5884, Jul. 2019.
- [14] K. Henken, D. Van Gerwen, J. Dankelman, and J. Van Den Dobbelsteen, "Accuracy of needle position measurements using fiber Bragg gratings," *Minimally Invasive Therapy Allied Technol.*, vol. 21, no. 6, pp. 408–414, Nov. 2012.
- [15] A. Gray, *Modern Differential Geometry of Curves and Surfaces With Mathematica*. Boca Raton, FL, USA: Chapman & Hall, 2006.
- [16] R. L. Bishop, "There is more than one way to frame a curve," *Amer. Math. Monthly*, vol. 82, no. 3, pp. 246–251, Mar. 1975.
- [17] K. O. Hill and G. Meltz, "Fiber Bragg grating technology fundamentals and overview," *J. Lightw. Technol.*, vol. 15, no. 8, pp. 1263–1276, Aug. 1997.
- [18] J. Van Roosbroeck, J. J. Vlekken, E. Voet, M. Voet, and C. Chojetzki, "A new methodology for fiber optic strain gage measurements and its characterization," in *Proc. SENSOR+TEST Conf. Opt. Fiber Sensors (OPTO)*, vol. 2, Nuremberg, Germany, May 2009, pp. 59–64.
- [19] R. C. Hibbeler, *Mechanics of Materials*, 8th ed. Upper Saddle River, NJ, USA: Prentice-Hall, 2011.
- [20] J. Cui, S. Zhao, C. Yang, and J. Tan, "Parallel transport frame for fiber shape sensing," *IEEE Photon. J.*, vol. 10, no. 1, pp. 1–12, Feb. 2018.
- [21] S. Umeyama, "Least-squares estimation of transformation parameters between two point patterns," *IEEE Trans. Pattern Anal. Mach. Intell.*, vol. 13, no. 4, pp. 376–380, Apr. 1991.
- [22] B. Van Hoe, J. Van Roosbroeck, C. Voigtlander, J. Vlekken, and E. Lindner, "Distributed strain and curvature measurements based on tailored draw tower gratings," in *Proc. IEEE Avionics Vehicle Fiber-Optics Photon. Conf. (AVFOP)*, Long Beach, CA, USA, Oct./Nov. 2016, pp. 285–286.
- [23] FBGS International NV. (Jan. 2019). *Draw Tower Gratings (DTG)*. Accessed: Jan. 7, 2020. [Online]. Available: <https://fbgs.com/components/draw-tower-gratings-dtgs/>
- [24] *Manual 'ILLumiSense' Software, Version 2.3*, FBGS Int., Bell Telephonaan 2H, Geel, Belgium, 2014.
- [25] T. Watts, R. Secoli, and F. R. Y. Baena, "A mechanics-based model for 3-D steering of programmable bevel-tip needles," *IEEE Trans. Robot.*, vol. 35, no. 2, pp. 371–386, Apr. 2019.
- [26] NDI Medical. (Sep. 2013). *Aurora-Medical*. Accessed: Jan. 7, 2020. [Online]. Available: <https://www.ndigital.com/medical/products/aurora/>
- [27] A. Leibinger *et al.*, "Soft tissue phantoms for realistic needle insertion: A comparative study," *Ann. Biomed. Eng.*, vol. 44, no. 8, pp. 2442–2452, Aug. 2016.
- [28] FBGS International NV. (Jan. 2019). *DTG & FSG Technology*. Accessed: Jan. 7, 2020. [Online]. Available: <https://fbgs.com/technology/dtg-fsg-technology/>